Thermal Fluctuations of Oriented Lipid Membranes by Nonspecular Neutron Reflectometry[†]

T. Salditt,*,[‡,||] C. Münster,[‡] U. Mennicke,[‡,||] C. Ollinger,[‡,||] and G. Fragneto[§]

Experimentalphysik, Universität des Saarlandes, 66041 Saarbrücken, Germany, and Institut Laue-Langevin, F-38043 Grenoble Cedex, France

We present a novel method to measure and to analyze lipid bilayer fluctuations based on time-of-flight nonspecular neutron reflectivity (TOF-NSNR). To validate this approach, we compare the results obtained on the phospholipid 1,2-dimyristoyl-*sn*-glycero-3-phosphatidylcholine (DMPC) to NSNR data collected in the conventional monochromatic mode. For the DMPC model system in its fluid L_α phase, we determine the fluctuation spectrum of an averaged bilayer in an oriented multilamellar stack and compare the result to the predictions of the linearized smectic free energy functional. In particular, we show how the smectic penetration depth Λ can be determined from the measurements. Furthermore, significant changes in the fluctuation spectrum of DMPC are observed upon the interaction with the antimicrobial peptide magainin 2 and cannot be explained by the smectic model.

I. Introduction

Thermal fluctuations of lipid membrane phases reflect fundamental physical properties of the lipid bilayer, related to thermodynamic stability, elasticity, interaction potentials, and phase transitions.[1] Reciprocally, fluctuations may strongly influence these phenomena, as well as different self-assembly properties of lipid membranes. If this interplay is quantitatively understood, more complex biomimetic membrane systems, consisting of lipid bilayers and additional membrane-active molecules such as membrane proteins or peptides, can be addressed. Thermal fluctuations in lipid bilayer phases have been probed by X-ray and neutron scattering with line shape analysis, carried out on aqueous bulk suspensions.[2] Multilamellar phases of stacked lipid bilayers exhibiting smectic liquid-crystalline symmetry have received particular attention.[2,3] They allow for a tremendous increase in scattering volume over single bilayer or more dispersed phases. Importantly, interaction potentials between neighboring membranes can also be inferred from such studies.[2,4,5] However, it is understood that the full information on the characteristic displacement correlation functions is lost due to powder averaging over the isotropic distribution function of domains in solution. Correspondingly, model assumptions have to be introduced in the data analysis, such as the Caillé or modified Caillé models derived from linear smectic elasticity theory. In this model, two elastic constants B and K govern the compressional and bending modes of the smectic phase, respectively. For large bilayer bending rigidity $\kappa \gg kT$ typical for phospholipid systems,[6] only the combination $\sqrt{KB}$ of the two Caillé moduli B and $K = \kappa/d$ can be inferred from the measured line shape exponent $\eta = \pi kT/(2d^2\sqrt{KB})$. The second fundamental parameter, the smectic penetration length $\Lambda = \sqrt{K/B}$, is usually not accessible, unless the bending rigidity becomes small, $\kappa \simeq kT$.[2]

Contrarily, the study of fluctuations in aligned (oriented) lamellar phases on solid substrates does not suffer from similar restrictions.[7] In such systems, specular and diffuse (nonspecular) X-ray (NSXR) and neutron reflectivity (NSNR) yield model-independent information on the height−height correlation functions.[8,9] In both cases, the nonspecular (diffuse) intensity distribution can be described by a structure factor $S(q_z, q_{||})$, measured as a function of the parallel and vertical component of the momentum transfer,[10] $q_{||} = (q_x^2 + q_y^2)^{1/2}$ and q_z, respectively. Here we present a novel method to measure and to analyze bilayer fluctuations based on time-of-flight (TOF) mode nonspecular neutron reflectivity (TOF-NSNR). For specular reflectometry, the advantages of TOF, in particular small accumulation times, have already been well established.[11] More generally, the approach allows the study of (dynamic) thermal fluctuations or static defects in aligned smectic phases. In particular, we show how the smectic penetration depth Λ (at least as an effective parameter) can be determined from the measurements. For comparison and to check the validity of the technique, we also present measurements carried out in the conventional monochromatic mode of NSNR.

There are two technical reasons for using NSNR (in addition to NSXR): First, the transparency of the solid substrate for neutrons gives access to a continuous range of parallel momentum transfer $q_{||} = (q_x^2 + q_y^2)^{1/2}$ at fixed vertical momentum transfer (e.g., for constant $q_z = 2\pi/d$),

---

[†] Part of the *Langmuir* special issue dedicated to neutron reflectometry.

[‡] Universität des Saarlandes.

[§] Institut Laue-Langevin.

[||] Present address: Inst. für Röntgenphysik, Geiststr. 11, D-37073 Göttingen, Germany.

(1) *Structure and Dynamics of Membranes*; Lipowsky, R., Sackmann, E., Eds.; Handbook of Biological Physics, Vol. 1A; Elsevier Science: Amsterdam, 1995; Vol. 1, Parts A & B.

(2) Safinya, C. R.; Sirota, E. B.; Roux, D.; Smith, G. S. *Phys. Rev. Lett.* **1989**, *62*, 1134; **1986**, *57*, 2718.

(3) Petrache, H. I., et al. *Phys. Rev. E* **1998**, *57*, 7014.

(4) Pabst, G.; Katsaras, J.; Raghunathan, V. A.; Rappolt, M. *Langmuir* **2003**, *19*, 1716.

(5) Rand, R. P.; Parsegian, V. A. *Biochim. Biophys. Acta* **1989**, *988*, 351 and references therein.

(6) In the absence of surfactants or alcohols (e.g., pentanol).

(7) Lyatskaya, Y.; Liu, Y.; Tristram-Nagle, S.; Katsaras, J.; Nagle, J. F. *Phys. Rev. E* **2000**, *63*, 011907.

(8) Salditt, T., et al. *Phys. Rev. E* **1999**, *60*, 7285.

(9) Salditt, T.; Vogel, M.; Fenzl, W. *Phys. Rev. Lett.* **2003**, *90*, 178101.

(10) Smith, G.; Sirota, E. B.; Safinya, C. R.; Clark, N. A. *Phys. Rev. Lett.* **1988**, *60*, 813.

(11) Thomas, R. K.; Penfold, J. *Curr. Opin. Colloid Interface Sci.* **1995**, *1*, 23 and references therein.

opening up the possibility to study fluctuations, on length scales between a few angstroms up to several micrometers, essentially in one scan.[16] Second, in TOF mode simultaneous collection of neutrons over a range of wavelengths $\lambda \in \{2...20 \text{ Å}\}$ becomes possible, significantly reducing accumulation time. Thus time-dependent measurements become possible, without the risk of radiation damage, as is important in the case of (white beam) energy-dispersive X-ray scattering. Finally, the option of contrast variation which is widely used in specular neutron reflectometry of lipid monolayers and bilayers[17,18] also applies to NSNR. Up to now, only relatively few studies have presented quantitative analysis of nonspecular (diffuse) scattering in TOF mode; for example, see refs 12−15. Therefore, the present report on TOF-NSNR includes some rather technical considerations of the experiment and data evaluation schemes.

In this study, we have concentrated on the well-known phospholipid 1,2-dimyristoyl-*sn*-glycero-3-phosphatidylcholine (DMPC). As a main result, we have quantified the fluctuation spectrum of DMPC as measured by nonspecular neutron reflectometry and have compared it to measurements in monochromatic mode both with neutrons and X-rays. The data are discussed in the framework of the linearized smectic free energy functional. In a second step, we have examined the phospholipid system with and without the antimicrobial peptide magainin 2. The addition of the peptide strongly affects the fluctuation spectrum of DMPC, as observed by mappings of reciprocal space in $q_{\parallel}$ and q_z.

The paper is organized as follows: After this introduction, the scattering theory is presented in section II, followed by the Experimental Section III. This section also discusses the raw data analysis, the conversion scheme, and the use of the novel D17 reflectometer at ILL, Grenoble, for TOF-NSNR. Section IV presents the results obtained on DMPC, with a technical focus on TOF-NSNR. The technique and the results are then compared to those of nonspecular X-ray reflectivity and monochromatic neutron reflectometry. Section V is devoted to results obtained on magainin 2 interacting with DMPC. These results have been obtained in the more conventional monochromatic mode. The paper closes with a short summary and outlook.

II. Linear Smectic Elasticity Theory and Nonspecular Scattering

Multilamellar membrane fluctuations are typically described by the linearized free energy density of a 3D smectic liquid crystal.[19] In reciprocal space, smectic elasticity theory predicts pronounced power-law peak line shapes as a result of diverging positional correlations in an infinitely large system (Landau−Peierls instability). Accordingly, the intensity decays as $S(q_z - q_{z,n}) \propto (q_z - q_{z,n})^{-(2-\eta_n)}$ with $q_{z,n}$ denoting the center of the nth-order peak. From the measurement of the powder-averaged structure factor, one can determine usually only one combination of the smectic constants K and B, and only

in rare cases both constants independently.[2] Furthermore, in many samples, limited domain size (or finite-size effects) may undermine the correct assessment of the power-law line shape in the vicinity of the peaks. In principle, the finite size D in the stacking (z) direction should remove the singularity at $q_{z,n}$ and leads to a peak line shape which can be described by a superposition of a sharp Bragg-like component and the above power-law singularity.[20,21] Experimentally, "real-structure" effects make it particularly important to probe $S(q_z, q_{\parallel})$ over a wide range and at a high signal-to-noise ratio.

This can be achieved by the use of highly oriented films, where the diffuse scattering can be probed over a wide range, independently as a function of both $q_{\parallel}$ (corresponding to the xy-plane of the membrane, see Figure 1) and q_z. On large length scales, the finite-size effects and the presence of film boundaries (e.g., at the substrate) become apparent. Contrarily, on short length scales the bilayers do not necessarily fluctuate in unison, as is assumed in the classical treatment of smectic elasticity using a continuum displacement field $u(r, z)$.[21,23,24] To describe the fluctuations on length scales ranging from the mesoscopic scale down to molecular length scales, the discrete version of the free energy functional (Hamiltonian) must be considered, which can be written as[20]

$$H = \int_A \mathrm{d}^2 r \sum_{n=1}^{N-1} \left(\frac{1}{2} \frac{B}{d} (u_{n+1} - u_n)^2 + \frac{1}{2} \kappa (\nabla_{xy}^2 u_n)^2 \right) \quad (1)$$

where κ denotes the bilayer bending rigidity, A the area in the xy-plane, N the number of bilayers, and u_n the deviation from the mean average position nd of the nth bilayer. B and $K = \kappa/d$ are elastic coefficients, governing the compressional and bending modes of the smectic phase, respectively. Equation 1 is called the discrete smectic Hamiltonian, in contrast to the continuum (Caillé) model, where the sum over n is replaced by an integral. Film boundaries can be accounted for by surface tension terms, which are not included above. From a complete treatment of free-standing smectic films including surface tension γ, it can be shown that the surface tension defines a lateral length scale $R_1 \simeq (D\Lambda/\ln|(1 + \nu)/(1 - \nu)|)^{1/2}$, where $\nu = \gamma/\sqrt{KB}$ and γ is the surface tension.[22] For $r \ll R_1$, the fluctuations are not affected by the film boundaries, and hence also not by γ. Contrarily, for $r \gg R_1$, the top and bottom layer fluctuate in unison with an amplitude governed by γ. For thick smectic films with a few thousand layers (or bilayers) and thickness $D \simeq 5-10$ μm, R_1 thus becomes very large. Moreover, for fully hydrated lipids $\gamma \rightarrow 0$, so that γ should not be relevant. However, the presence of the flat substrate forces the bottom bilayer to be flat on large length scales, which can be treated as an infinite surface tension. Therefore, fluctuations on length scales smaller than $\xi_{max} \simeq \sqrt{D\Lambda}$ should not be excited. Thus we include boundary effects in the present treatment only in the form of a low $q_{\parallel}$ cutoff. A more rigorous approach is to calculate the correlation function explicitly in the presence of a flat substrate.[25,26]

(12) Pynn, R. *Phys. Rev. B* **1992**, *45*, 602.
(13) Felcher, G., et al. *Phys. Rev. B* **1994**, *50*, 9565.
(14) Langridge, S., et al. *Phys. Rev. Lett.* **2000**, *85*, 4964.
(15) Li, Z. X.; Lu, J. R.; Thomas, R. K.; Weller, A.; Penfold, J.; Webster, J. R. P.; Sivia, D. S.; Rennie, A. R. *Langmuir* **2001**, *17*, 5858.
(16) Münster, C.; Salditt, T.; Vogel, M.; Peisl, J. *Europhys. Lett.* **1999**, *46*, 486.
(17) Bayerl, T. M.; Thomas, R. K.; Rennie, A.; Penfold, J.; Sackmann, E. *Biophys. J.* **1991**, *60*, 1.
(18) Kuhl, T. L., et al. *Biophys. J.* **1998**, *75*, 2352.
(19) Helfrich, W. *Z. Naturforsch.* **1973**, *28c*, 693.

(20) Lei, N.; Safinya, C. R.; Bruinsma, R. *J. Phys. II France* **1995**, *5*, 1155. Lei, N. Ph.D. Thesis, Rutgers, New Brunswick, NJ, 1993.
(21) Caillé, A. *C. R. Acad. Sci. B* **1972**, *274*, 891.
(22) Mol, E. A. L., et al. *Phys. Rev. E* **1996**, *54*, 536.
(23) Als-Nielsen, J., et al. *Phys. Rev. B* **1980**, *22*, 312.
(24) Holyst, R.; Tweet, D. J.; Sorensen, L. B. *Phys. Rev. Lett.* **1990**, *65*, 2153.
(25) Shalaginov, A. N.; Romanov, V. P. *Phys. Rev. E* **1993**, *48*, 1073.
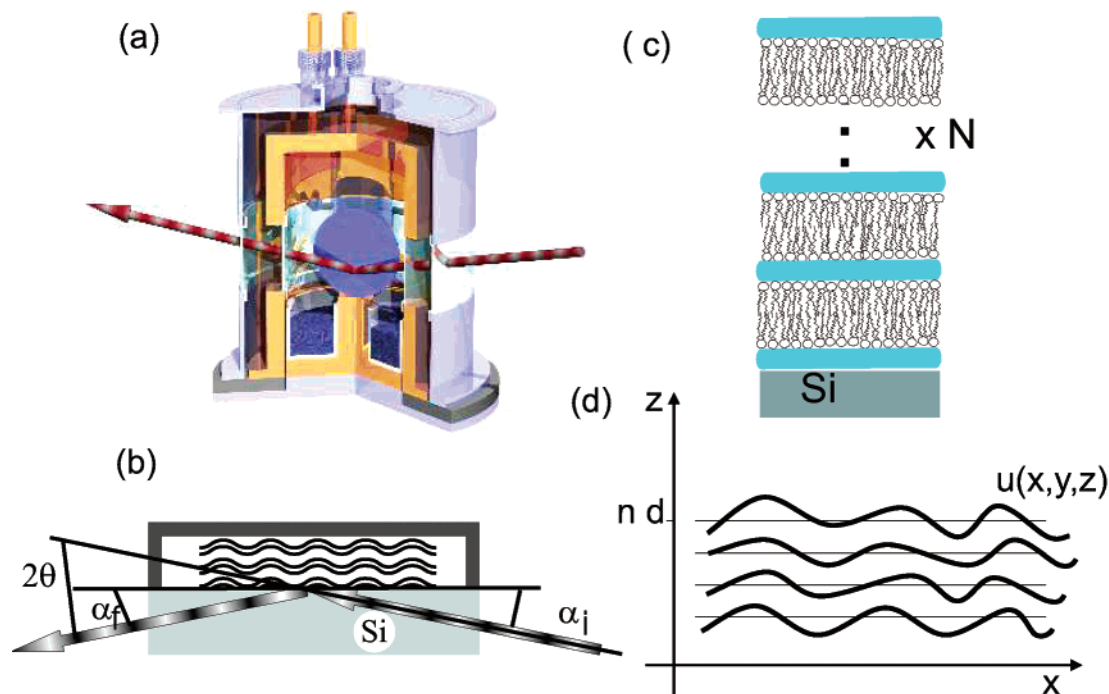(26) Constantin, D.; Mennicke, U.; Li, C.; Salditt, T. *Eur. Phys. J. E*, submitted.

Figure 1. (a) A sketch of the chamber used for the measurements where the incident beam of neutrons impinges on the solid-supported bilayers at grazing angles α_i, scanning continuously from positive to negative α_i (from above or from the side of the silicon substrate). The sample is exposed to saturated vapor pressure and should nominally be at 100% relative humidity. However, due to small gradients in T, only about 98% relative humidity is reached. (b) A sketch of the beam path in a chamber operating at full hydration with the bilayers immersed in excess water. Alternatively, an optimized design of the chamber shown in panel a with separate T-control of the sample and water bath can also warrant full hydration from water vapor. (c) A sketch of the solid-supported bilayers separated by a water layer of a thickness which is controlled by the relative humidity and which in the case of DMPC is at most $\simeq24$ Å thick. (d) Coordinate system and parametrization of the height displacement field $u(x, y, z)$ used in the text.

From eq 1, the height−height (displacement) correlation function is calculated as[20]

$$g(r, z) = \frac{\eta}{\pi^2}d^2 \int_0^\infty dq_\parallel \frac{(1 - J_0(q_\parallel r) \exp(-\Lambda z q_\parallel^2))}{q_\parallel \sqrt{1 + \frac{Kd^2}{4B}q_\parallel^4}} \quad (2)$$

where the exponent $\eta = \pi kT/(2d^2\sqrt{KB})$, $\Lambda = \sqrt{K/B}$, and J_0 is the Bessel function of first kind and zero order. Contrarily, in the framework of the continuous model according to Caillé, one obtains for $g(r, z)$[21,23]

$$g(r, z) = \frac{\eta}{\pi^2}d^2 \int_0^{2\pi/l} dq_\parallel \frac{(1 - J_0(q_\parallel r)) \exp(-\Lambda z q_\parallel^2)}{q_\parallel} \quad (3)$$

The height−height self-correlation function $g(r) = g(r, z = 0)$ is a special case which is of particular interest. Expressed in natural units $R = r/\xi_s$, $G(R) = g(R)/(\eta d^2/2\pi^2)$ can be approximated by $G(R) = R^2(1.11593 - \ln[R])$ for small $r \le \xi_s$ and by $G(R) = \ln[R^2] + 1.15443$ for $r \ge \xi_s$. The approximations are correct to within less than about 5% over the full range of R, when compared with the exact but computationally more difficult correlation function of eq 1. $\xi_s = \sqrt{\Lambda d}$ is a crossover length scale below which the bilayer fluctuates independently from its neighbors like a single membrane. In this regime, the continuum Caillé model breaks down. In the opposite limit $r \ge \xi_s$, $g(r)$ diverges logarithmically as is well-known from the continuum model of smectic elasticity.

Independent of any specific model describing the equilibrium or nonequilibrium bilayer fluctuations, the statistical height−height difference functions (or correlation functions) can be written as $g_{ij}(r) = \langle[u_i(\mathbf{r}') - u_j(\mathbf{r}'+$

$\mathbf{r})]^2\rangle$, where u denotes the deviation from the mean average position of the bilayer labeled by i and j.[27] The correlation functions are characterized by two length scales, corresponding (a) to the maximum lateral wavelength of fluctuations ξ_{max} and (b) the vertical length scale ξ_z over which the fluctuations of wavelength ξ_{max} are correlated, defining the conformality. The two length scales are related: In a film of finite thickness D on a flat substrate, equilibrium fluctuations are only excited on a length scale $r \le \xi_{max}$, see above. On length scales $r > \xi_{max}$, the bilayers are essential flat, since the associated smectic damping length $\xi_z \simeq \xi_{max}^2/\Lambda$ excludes a corresponding relaxation of the profile within the film thickness D. On small length scales $r \ll \xi_{max}$, the fluctuations are not affected by the film boundaries and should be described by bulk smectic theory.

Let σ denote the root-mean-square (rms) amplitude of the bilayer fluctuations measured on the lateral length scale ξ_{max}. The diffuse scattering measured in the plane of reflection can be written as a unique transformation of $g_{ij}(r) = 2\sigma^2 - 2c_{ij}(r)$, by[27]

$$S(q_x, q_z) = \frac{L_x L_y}{q_z^2} \sum_{i,j}^N \Delta\rho^2 \, e^{-q_z^2\sigma^2} \, e^{-iq_z(h_i-h_j)} \, \epsilon_{ij}(\mathbf{q}) \quad (4)$$

with

$$\epsilon_{ij}(\mathbf{q}) = \int dr r \, (e^{q_z^2 c_{ij}(r)} - 1) \cos(q_x r) \quad (5)$$

where $\Delta\rho$ is the effective scattering length contrast

(27) Sinha, S. K.; Sirota, E. B.; Garoff, S.; Stanley, H. B. *Phys. Rev.* **1988**, *B 38*, 2297. Sinha, S. K. *J. Phys. III (France)* **1994**, 4.

between the bilayer and D_2O,[28] L_xL_y is the illuminated area, and σ is the rms fluctuation amplitude. In the derivation, the diffuse scattering is integrated over the direction perpendicular to the plane of incidence (hence over q_y), as in the present experiment. For a pointlike detector slit setting, the term $\cos(q_x r)$ has to be replaced by $J_0(q_{\parallel} r)$ with $q_{\parallel}^2 = q_x^2 + q_y^2$.

Inserting the height–height cross-correlation function corresponding to the smectic model in the scattering equations (eqs 4 and 5), precise predictions on the observable scattering distribution can be made. In the following experiment, we consider two characteristic quantities: (i) the cross-correlation length $\xi_z(q_{\parallel})$ defining the length scale over which a thermal mode is correlated as a function of the corresponding wavevector $q_{\parallel}$ and (ii) the decay of the q_z-integrated diffuse scattering with $q_{\parallel}$, that is, the structure factor of the fluctuations. The cross-correlation function and the parameter ξ_z can be deduced from the peak line shape and width (half-width at half-maximum (HWHM)) along q_z. A Lorentzian line shape indicates an exponential decrease of the cross-correlations along z with a characteristic length scale $\xi_z = 1/HWHM$. Since the HWHM increases with $q_{\parallel}$, ξ_z depends on the wave vector of the height fluctuations, or conversely, the lateral length scale of the fluctuation. Linear smectic elasticity predicts $\xi_z = 1/(q_{\parallel}^2 \Lambda)$.[29]

III. Experimental Section

DMPC was bought from Avanti, Alabaster, AL, and was used without further purification. Magainin 2 amide (*GIGKFLH-SAKKFGKAFVGEIMNS*) was synthesized by B. Bechinger and co-workers by solid-phase peptide synthesis using an automated peptide synthesizer and Fmoc chemistry, as described elsewhere.[30] The peptide was purified by reversed phase high-performance liquid chromatography (HPLC) and a water/acetonitrile gradient in the presence of 0.1% trifluoroacetic acid. The high purity of the peptides was controlled by matrix-assisted laser desorption mass spectrometry (MALDI-MS). Multilamellar bilayers were prepared on cleaned 2 in. silicon wafers ((111) or (100) orientation) by spreading from organic solution.[31,32] For the measurements on samples immersed in water, 1 cm thick, polished 2 in. silicon blocks (SESO, France) were used. In such thick sample substrates, the neutron beam can be coupled into the substrate without refraction from the side. The beam then impinges at grazing incidence onto the sample with the incoming and reflected beam path in silicon rather than in water, avoiding incoherent scattering in H_2O or D_2O/H_2O mixtures, see Figure 1b.

For sample deposition, the substrates were cleaned, rendered hydrophilic, and positioned in an exactly horizontal plane. The wafers were cleaned by subsequent washing in methanol and ultrapure water (specific resistivity $\geq$ 18 MΩ cm, Millipore, Bedford, MA) and made hydrophilic by washing in a 5 M solution of KOH in ethanol for about a minute, or alternatively by plasma etching. The lipid and peptide components were codissolved in the desired ratio (molar ratio P/L) in trifluoroethanol (TFE) or (1:1) TFE–chloroform mixtures at concentrations between 10 and 40 mg/mL, depending on the total mass to be deposited. Pure DMPC was also deposited from 2-propanol. A drop of 1 mL was then carefully spread onto the well-leveled and cleaned 2 in.

substrates, yielding film thicknesses of about $D \simeq 5-20\ \mu m$, see Figure 1c. After a slow evaporation process avoiding film rupture, remaining traces of solvent in the sample were removed by exposing the samples to a high vacuum overnight. The films were then rehydrated in a hydration chamber and tempered above the main phase transition. The orientational alignment of the multilamellar stack with respect to the substrate (mosaicity) was typically better than 0.01°. A very low mosaicity is a prerequisite to apply interface-sensitive scattering techniques. The lateral domain sizes were in the range of 100 μm, exhibiting a broad distribution in the total number N of the bilayers. The low mosaicity was preserved after immersing the samples in water.

During the experiments, the solid-supported multilamellar films were kept in different temperature- and hydration-controlled chambers. For the neutron measurements carried out at partial hydration with the bilayers facing D_2O vapor, a chamber with two concentric high-purity aluminum cylinders was used, see Figure 1a. The inner cylinder was heated or cooled by a flow of oil, connected to a temperature-controlled reservoir (Julabo, Germany) with PID-control. The space between the two cylinders was evacuated to minimize heat conduction. The temperature was measured close to the sample holder by a Pt100 sensor, indicating a thermal stability of better than 0.02 K over several hours. At the bottom of the inner cylinder, a water reservoir was filled with salt-free Millipore water, such that the sample was effectively facing a vapor phase of nominally 100% relative humidity. Despite the nominally full hydration condition, the DMPC bilayers were typically swollen only up to a repeat distance of only $d \simeq 50-55$ Å in the fluid L_{α} phase, that is, were only partially hydrated. This limited swelling of solid-supported lipid films is well-known as the so-called vapor-pressure paradox and has recently been explained by Katsaras and co-workers on the basis of small temperature gradients in the chamber.[33] Accordingly, it was demonstrated that chambers of suitable design do not show this effect and that bilayers can be swollen to equilibrium (full hydration) from the vapor phase. We have also used a chamber which allows for full hydration without immersing the sample in water (used in the present TOF-NSNR experiment on D17/ILL), as evidenced by the well-known equilibrium d spacing for DMPC. This is achieved by a design where the temperature of the water bath can be separately controlled and a small difference in the temperature of the bath with respect to that of the sample leads to full hydration. At the Adam reflectometer (operating in monochromatic mode), we have used a humidity chamber which can swell DMPC bilayers up to 50–55 Å, thus corresponding to partial hydration. Alternatively, we have used a chamber operating at full hydration, where the bilayers are immersed in water, and the beam impinges through a thick Si block, see Figure 1b. This setup is the neutron analogue of the X-ray chamber used in a recent temperature-dependent study of specular reflectivity on aligned lipid bilayers.[34] Conditions of full hydration are important, since the diffuse (nonspecular) scattering from partially hydrated films may be affected by static defects and the associated strain fields,[8] rather than by thermal diffuse scattering. Furthermore, it is desirable to probe the elasticity and fluctuation properties in the physiologically relevant state of full hydration.

The experiments were carried out at the Adam reflectometer using monochromatic neutrons of wavelength $\lambda = 4.4$ Å[16,36] and at the new D17 reflectometer of ILL, Grenoble, in TOF mode.[37] TOF allows for a specular and nonspecular reflectivity experiment, in which neutrons with a broad range of wavelength λ are used simultaneously and registered as a function of their respective times of flight. The diffracted intensity can be recorded on a two-dimensional detector as a function of q_z and q_x without moving any motors. The necessary pulsing of the beam is realized by a double chopper system set to a rotational speed of 1000 rpm and a projected sector opening of 2.2° and 5°, respectively,

(28) More generally, the whole scattering length profile across one lamellar unit of length d is accounted for by a multiplicative form factor.

(29) An easy way to derive the relationship $\xi_z = 1/(\Lambda q_{\parallel}^2)$ is to consider the elastic response of the multilamellar stack to the given perturbation of one bilayer. The perturbation is relaxed in the neighboring bilayers by a combination of bending and compression modes, leading to an extended distortion field. Assuming a sinusoidal profile, the associated distortion field can be written as $u = u_0 \exp(-|z - z_0|/\Lambda(q_{\parallel}) \cos(q_{\parallel}r)$ with a damping length $(\Lambda q_{\parallel}^2)^{-1}$ along z.

(30) Bechinger, B. *Biochim. Biophys. Acta* **1999**, *1462*, 156–183 and references therein.

(31) Seul, M.; Sammon, M. J. *Thin Solid Films* **1990**, *185*, 287.

(32) Mennicke, U.; Salditt, T. *Langmuir* **2002**, *18*, 8172.

(33) Nagle, J. F.; Katsaras, J. *Phys. Rev. E* **1999**, *59*, 7018.

(34) Vogel, M., et al. *Phys. Rev. Lett.* **2000**, *84*, 390.

(35) Vogel, M. Ph.D. Thesis, Universität Potsdam, Potsdam, Germany, 2000.

(36) Schreyer, A.; Siebrecht, R.; Englisch, U.; Pietsch, U.; Zabel, H. *Physica B* **1998**, *248*, 349.

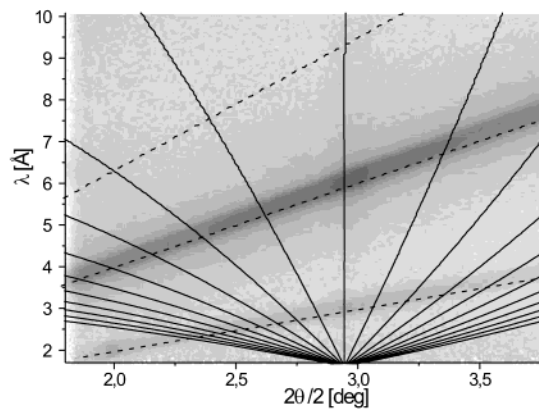(37) Cubitt, R.; Fragneto, G. *Appl. Phys. A* **2003**, *74*, 329.

Figure 2. Typical intensity distribution (logarithmically scaled gray shades) observed on the detector at D17 in TOF mode for a DMPC sample in the fluid L_α phase, as a function of scattering angle 2θ (calculated from the horizontal pixel number) and neutron wavelength λ calculated from the time of flight. The angle of incidence $\alpha_i = 2.9°$.

depending on the desired resolution. Here, the small opening angle was used at small angles of incidence $\alpha_i \leq 1°$, when the collimating slits were set to give a small beam of 0.4 mm (horizontal) at the sample positions, while the larger opening angle was used for all incidence angles $\alpha_i \geq 1°$, when the collimating slits were set to a beam of 2.5 mm at the sample. This way, the beam size was matched to the acceptance of the sample (deposited on 2 in. Si blocks) at the respective angles α_i. A multiwire proportional counter with 256×256 pixels (delay-line, Gabriel, EMBL Grenoble) was positioned 3.4 m behind the sample, equipped with an evacuated flight path.

In TOF mode, the intensity matrix is obtained as follows: First, the counts are registered for each spatial pixel (x, y) as a function of TOF in 500 channels. Next, the counts are integrated for fixed x and TOF channel along the vertical detector axis y, yielding a 2D array of $I[x, \text{TOF channel}]$. The data array can then be further analyzed by the instrument's LAMP software or saved in ASCII and processed by one's own data analysis programs as in the present case. For this purpose, a calibration file ([2, 500]-matrix) must first be computed by LAMP for the TOF/λ conversion. The data are then read by a MATLAB routine, performing (i) the TOF/λ conversion, (ii) a correction for detector sensitivity (spatial variation of pixel sensitivity as a function of x, as measured by incoherent scattering from H_2O), (iii) division by the λ-distribution, as measured by shots of the direct beam under identical chopper and slit settings, and (iv) a conversion from x-pixel to scattering angle 2θ. Finally, the corrected data set $I[\theta, \lambda]$ can also be transformed to $I[q_z, q_x]$ with a given (constant) angle of incidence α_i. However, to minimize regridding errors, we chose to work with the representation $I[\theta, \lambda]$ and to convert to **q** space only in the last step when 1D data sets have been computed by the appropriate cuts and slices in the 2D data set.

Figure 2 shows a representative 2D data set $I[\theta, \lambda]$ for a multilamellar stack of DMPC in the fluid L_α phase at $T = 40°$ C, obtained at a fixed detector position and $\alpha_i = 2.94°$, in logarithmically scaled gray shades. The different columns of the multiwire detector matrix correspond to different scattering angles 2θ, with $2\theta = \alpha_i + \alpha_f$ (for convention of angles names, see also Figure 1b). Enhanced diffuse scattering stemming from correlated thermal fluctuations is observed at the position of the diffuse Bragg sheets, for all wavelengths λ and detector angles 2θ, satisfying the position of the first two diffuse Bragg sheets $q_z = 2\pi/d$ and $q_z = 4\pi/d$ (higher order Bragg sheets are not observed in the angular and wavelength range covered). The diffuse Bragg sheets appear as a straight line at oblique angles. Indeed, curves of constant q_z appear as a bunch of divergent lines intersecting at the origin (see dashed lines in Figure 2) and are given in small-angle approximation by $\lambda = 2\pi(2\theta)/q_z$, while curves of constant q_x are given in small-angle approximation by the parabolas $\lambda = \pi(2\theta - \alpha_i)^2/q_x - \pi\alpha_i^2/q_x$ (see solid lines in Figure 2). One column of the matrix corresponding to $2\theta = 2\alpha_i$ defines the specular axis; its intersection with the diffuse Bragg sheets

defines the specular Bragg peaks, which are enhanced over the diffuse Bragg sheets due to the specular component. From these positions, a lamellar periodicity $d = 59$ Å is obtained. Quantitative information on the height–height correlation functions can now be obtained by evaluating the intensity matrix along the different principal axes, for example, along the horizontal $2\theta/2$ and vertical λ axis. To extend the angular range in 2θ, matrices obtained at different detector positions are combined.

IV. Analysis of Diffuse Scattering and Thermal Fluctuations of Pure DMPC

We first consider the decay of the Bragg sheet intensity with q_x. As we have shown previously, it is instructive to look at the q_z-integrated Bragg sheet intensity $\tilde{S}(q_\parallel) = \int_{BZ} dq_z S(q_z, q_\parallel)$, where BZ denotes one Brillouin zone $2\pi/d \pm \pi/d$. In this case, it can be shown that the contributions of the cross-correlation terms in eq 4 cancel, and one is left with a curve, which corresponds to the transform of an average height–height self-correlation function or the effective single-bilayer structure factor $\tilde{S}(q_\parallel)$.[42] In many cases, a power-law behavior is observed at high $q_\parallel$, indicating a corresponding algebraic regime of the real-space correlation function at small r. For TOF neutron scattering, we must integrate over λ rather than q_z. We therefore divide the data set $I(2\theta, \lambda)$ by λ^2 before integrating the intensity over λ for each constant angle 2θ. Since $dq_z = -2\pi/(\lambda^2) (\sin \alpha_i + \sin(2\theta - \alpha_i)) d\lambda$, we see that for constant α_i and 2θ, we have $dq_z \propto -1/(\lambda^2) d\lambda$. An additional factor λ enters from the conversion between the out-of-plane angle (in the vertical plane) and dq_y. The result corresponding to $\int_{peak} d\lambda \ S(2\theta, \lambda)/(\lambda^2) \ \lambda \propto \tilde{S}(q_x)$ can then be plotted as a function of q_x, which in turn is calculated from 2θ.

Figure 3 shows this curve (open circles) along with a simulation of the discrete smectic model according to eqs 2–5, for the integrated intensity of the first Bragg sheet. The DMPC bilayers were swollen to $d \simeq 60$ Å and kept at $T = 40$ °C in the fluid L_α phase. The parameters of the simulation are $\Lambda = 40$ Å, $\xi = 2000$ Å, and $q_z\sigma = 0.83$. A Gaussian peak has been added to account for the specular peak observed at small q_x. Note that the specular beam is separated from the diffuse Bragg sheet. Along with the results of the TOF experiment, two scattering curves measured on DMPC in the monochromatic mode at the Adam reflectometer are shown. The first one (circular dots) corresponds to a sample of partial hydration at $d = 50$ Å, for which scattering was particularly strong, allowing for a spectrum which extends almost to $q_x \simeq 0.1$ Å^{-1}. Note that at partial hydration the Bragg sheets are typically much stronger due to the enhanced ordering of bilayers along z. Also shown is a curve obtained on fully hydrated DMPC (immersed in a water cell, see ref 38) (open squares). The data measured in monochromatic mode at the Adam reflectometer show intensity modulations at positions where the incident beam is parallel to the sample horizon due to refraction effects. These purely optical effects have not been corrected for, but they can be completely described

(38) Münster, C. Ph.D. Thesis, Sektion Physik, Universität München, München, Germany, 2000.

(39) A quadratic increase of the HWHM in q_z with $q_\parallel$ can be modelled as $S(q_z, q_x, q_y) \propto 1/(q_z^2 + \Lambda^2(q_x^2 + q_y^2)^4)$. We now integrate over q_y corresponding to the experimental situation of a highly divergent beam and large slits in the vertical (y) direction. After integration of $S(q_z, q_x) \propto \int dq_y \ 1/(q_z^2 + \Lambda^2(q_x^2 + q_y)^4)$, we have numerically verified that HWHM-(q_x) still is a quadratic function, but with a coefficient which is larger than Λ by a factor of $1.41 \simeq \sqrt{2}$, so that HWHM$_{q_z} = (\sqrt{2})\Lambda q_x^2 = \Lambda_x q_x^2$.

(40) Ludtke, S.; He, K.; Huang, H. *Biochemistry* **1995**, *34*, 16764.

(41) Sens, P.; Turner, M. S. *J. Phys. II France* **1997**, *7*, 1855; *Phys. Rev. E* **1997**, *55*, R1275.

(42) Salditt, T., et al. *Phys. Rev. Lett* **1994**, *73*, 2228; *Phys. Rev. B* **1996**, *54*, 5860; *Phys. Rev. B* **1996**, *54*, 5860.
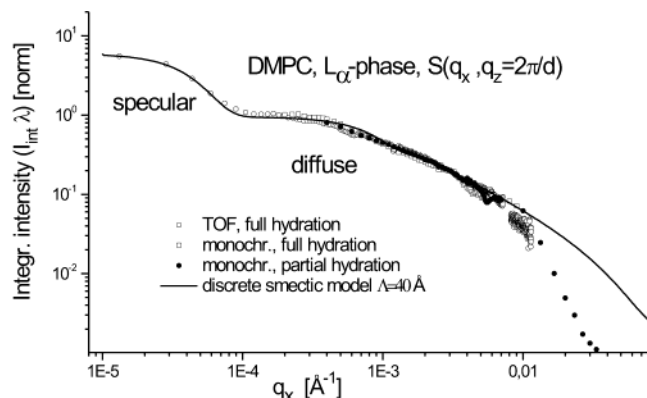
Figure 3. Diffuse structure factor $S(q_x, q_z = 2\pi/d)$ of DMPC in the fluid L_α phase. The data of the TOF experiment (open circles) are obtained by integration of the intensity of the Bragg sheets (shown in Figure 2) over λ and converting 2θ to q_x, after correcting for the prefactors associated with the coordinate transformation, as described in the text. The data points are superimposed to data obtained in the more conventional monochromatic mode (Adam reflectometer, open squares and solid circles), demonstrating that both experimental schemes yield consistent results. Also shown is a simulation of the discrete smectic model according to eqs 2–5 (solid line).

as shown in ref 16. Note that all curves overlap reasonably well at low and medium q_x and can be described fairly well by the smectic model (solid line) except at high q_x. This regime, however, has only been reached in the data taken on partially hydrated DMPC (see also ref 16), since the scattering intensity was highest in this case. Systematic deviations of the observed intensity decay (power law) for $q_x > 0.001$ Å^{-1} at high $q_\parallel$ have independently been found in diffuse X-ray studies of oriented bilayers, measured at full hydration, and may point to protrusion modes governing the fluctuations at small distances in the plane of the bilayer. The corresponding fluctuations, which are probably distinctly different from bending modes, still exhibit cross-correlations between neighboring bilayers, since the HWHM of the Bragg sheet remains finite. In fact the full width at half-maximum (FWHM) values saturate at $q_x \geq 0.01$ Å^{-1} (not shown). An alternative explanation could be related to a bending stiffness κ, which itself may depend on $q_\parallel$. Note however that before more conclusions can be drawn, the quantitative comparison should be made to the predictions of the smectic model taking into account the boundary effect of the flat substrate.[26]

We now analyze the width of the first Bragg sheet, that is, the HWHM along λ, and the increase in the HWHM as one moves further away from the specular line, that is, the broadening of HWHM$_\lambda$ with q_x. As we have shown before in monochromatic X-ray and neutron scattering, the vertical cross-correlation length $\xi_z(q_\parallel)$ of thermal fluctuations can be inferred from the analysis of the Bragg sheet width in q_z as a function of $q_\parallel$: $=(q_x^2 + q_y^2)^{1/2}$, that is, from HWHM$_{q_z}(q_\parallel)$. The conversion between HWHM$_\lambda$ and HWHM$_{q_z}$ is straightforward according to d$q_z/q_z = -$dλ/λ. The prediction of the smectic Hamiltonian in eq 1 is HWHM$_{q_z} = \Lambda q_\parallel^2$. Representative cuts along λ for different constant values 2θ are shown in Figure 3a, along with least-squares fits to the predicted Lorentzian line shape, yielding the peak width for each angle 2θ. In Figure 3b the peak width (HWHM) is then shown as a function of $\theta = 2\theta/2$. The characteristic broadening with increasing θ away from the specular peak at $\theta = \alpha_i = 1.6$ deg is very well described by an empirical parabolic least-squares fit (solid line) HWHM$_\lambda$/(Å) $= 0.188 - 0.139(\theta/\text{deg}) + 0.0432 (\theta/\text{deg})^2$.

Leaving the empirical fit aside, what is the function predicted by the linear smectic model? Since for the Lorentzian line shape, the intrinsic width and the resolution simply add, we have HWHM$_\lambda = (\tilde{\Lambda}_x q_x^2 + \Delta q z_0)\lambda/q_z$. The last factor arises from the λ/q_z conversion. The constant offset $\Delta q z_0$ takes into account finite resolution as well as the fact that the width of the Bragg sheet remains always finite at $q_x = 0$ (even if measured with an ideal instrument), due to finite-size effects. Interestingly, the dashed curve shown in Figure 4b corresponding to $\Lambda_x = 45$ Å and $\Delta q z_0 = 0.001$ Å^{-1} approximates the experimental data but shows some systematic deviations, which are not present in the empirical fit. This may eventually be a problem of resolution, which has been taken into account in an oversimplified manner. In TOF, the resolution in λ clearly depends on λ,[37] which we find difficult to quantify.

A further point to consider is the fact that the diffuse scattering has been integrated over q_y corresponding to the experimental situation of a highly divergent beam and large slits in the vertical (y) direction. As we have found by numerical simulation (for a special choice of the structure factor), this does not change the quadratic behavior of HWHM$_{q_z} \propto \Lambda_x q_x^2$, but leads to a different prefactor $\Lambda_x = (\sqrt{2})\tilde{\Lambda}$.[39]

In summary, we find reasonable agreement for $\Lambda \simeq 32$ Å as the only physical parameter, corresponding well with the value of 30 Å determined by nonspecular X-ray reflectivity for fully hydrated DMPC at T = 40 °C. However, some systematic errors are observed, probably due to the fact that the resolution of the instrument has not been taken into account correctly. To further support the validity of the TOF-NSNR method and the associated data analysis, a comparison with monochromatic data is shown in Figure 5b. For better control of the resolution effects, we propose the development of calibration standards with known propagation of fluctuations (e.g., based on multilayered samples deposited on static gratings with known propagation constants). We stress that the TOF mode has the potential of a very high resolution in q_z width analysis, also compared to synchrotron-based X-ray scattering. We are not aware of any measurements where smaller Bragg sheets could be measured than the present values.

In the monochromatic mode, the data can directly be measured as a function of q_z and q_x (reciprocal space mapping), that is, corresponding to an intensity matrix $I[q_x, q_z]$, using *hkl*-mode (mesh scans) of the Spec diffractometer software (Certified Scientific Software, Cambridge MA) installed at the Adam reflectometer. A typical data set is shown in Figure 5a in logarithmic color code for fully hydrated DMPC at $T = 45°$. The corresponding values (open circles) of HWHM(q_x) and the q_z-integrated structure factor $S(q_x)$ are shown in Figure 5b, along with other values obtained from monochromatic neutron scattering (at two different hydration states, open triangles and open squares). For comparison, the results of a recent synchrotron X-ray study are also shown,[9,35] as well as the data points of the TOF experiments transformed to q_x, q_z. Note that the curves HWHM(q_x) never go to zero for $q_x \rightarrow 0$, due to the intrinsic resolution-limited width (instrument, finite size of the sample). Therefore, the curves of the monochromatic neutron and X-ray scattering experiments have been shifted vertically to the value of the TOF result to compare the slope of the (parabolic) increase. Note also that the monochromatic neutron data have only been plotted up to the value of q_x which corresponds to the reflection (not transmission) case, since these data are flawed by refraction effects in the transition zone between reflection and transmission, approximately at the position
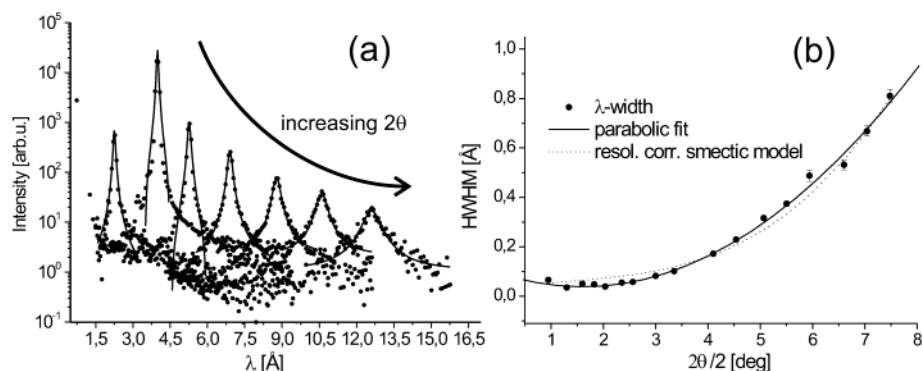
Figure 4. (a) Vertical cuts of the detector matrix (Figure 2), showing the intensity distribution of the first Bragg sheet as a function of λ for constant θ. The cuts can be fitted to a Lorentzian with HWHM values increasing with the distance away from the specular condition. The resulting HWHM values are plotted as a function of θ (b), along with an empirical parabolic fit (solid line) and the prediction of the smectic model (dashed line).
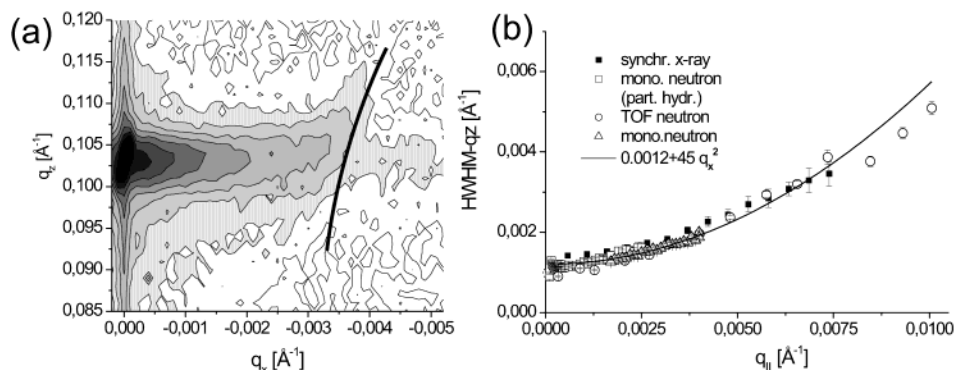

Figure 5. (a) Reciprocal space mapping of the first Bragg sheet measured with monochromatic nonspecular neutron reflectometry ($\lambda = 4.4$ Å, Adam). (b) The increase of the Bragg sheet width HWHM along q_z as a function of q_x. The data agree reasonably well for monochromatic and TOF data (converted from Figure 2b). The solid line is a simulation according to smectic elasticity theory.

of the sample horizon $\alpha_f = 0.$[16] Within these restrictions, the results agree fairly well, validating both the TOF-NSNR method and the assumptions of the linear smectic theory. However, statistical error analysis indicates underestimated statistical errors, or more likely remaining systematic errors, that is, the same as addressed above in Figure 4b.

Furthermore, at high q_x values, which have been measured only by synchrotron X-ray and monochromatic neutrons (in transmission, not shown), the function HWHM(q_x) saturates, which cannot be understood in the framework of smectic elasticity theory. We speculate that at these high q_x, the bending modes will be dominated by other collective molecular motions, possibly collective protrusion modes, or peristaltic modes of the bilayer. This could also explain the deviations in Figure 3 at the same (high) q_x values.

V. Change of Fluctuations by Added Antimicrobial Peptides: The Example of Magainin 2

Diffraction from highly aligned, multilamellar samples can be used as a sensitive probe for lipid−peptide interaction or more generally the interaction of bilayers with membrane-active molecules (such as stereols, peptides, and proteins). An active field of research is currently devoted to the understanding of the structure and functional mechanisms of short, amphiphilic peptides, which act as antibiotic and fungicidal agents in the immune system of vertebrates. The field has recently been reviewed by Bechinger[30] as well as other authors in the same issue. The amphipathic and antibiotic peptides interact directly with the microbial cell membranes rather

than with specific membrane proteins, subsequently causing an increase in membrane permeability and cell lysis. Huang and co-workers have studied aligned films of lipid−peptide model systems by X-ray and neutron diffraction as well as by circular dichroism spectroscopy and have reported a concentration-dependent phase transition from the parallel to an inserted state in several systems for the peptides alamethicin and magainin 2.[40] Magainin 2 belongs to this family of immunogenic peptides expressed in the skin and intestines of frogs. Most likely, the inserted state is linked to the formation of oligomeric pores. The phase transition has been described by a model in the framework of bilayer elasticity theory. Münster et al. have evidenced the strong decrease of short-range order in the acyl chains occurring already at moderate levels of peptide-to-lipid ratio P/L in the magainin 2/DMPC system.[16] Here we show that the diffuse scattering in a multilamellar lipid−peptide model system, in particular magainin 2/DMPC, changes significantly with P/L, indicating corresponding changes in the fluctuation and elasticity parameters, or perhaps also the defect structure of the lamellar phase.

Reciprocal space mappings $I[q_x, q_z]$ of the first Bragg sheet have been measured in monochromatic mode (Adam reflectometer, see also ref 38) at partial hydration in the fluid L_α phase for samples of different molar ratios P/L = 0, 0.02, 0.01, 0.033, and 0.05. Figure 6 shows the reciprocal space mappings for P/L = 0.02, 0.01, and 0.033, from top to bottom, in color-coded intensities (logarithmically scaled). Two effects become directly apparent even before any quantitative analysis: (i) The intensity of the Bragg sheet decreases with increasing P/L. (ii) The width (HWHM − q_z) of the Bragg sheet increases with P/L. The
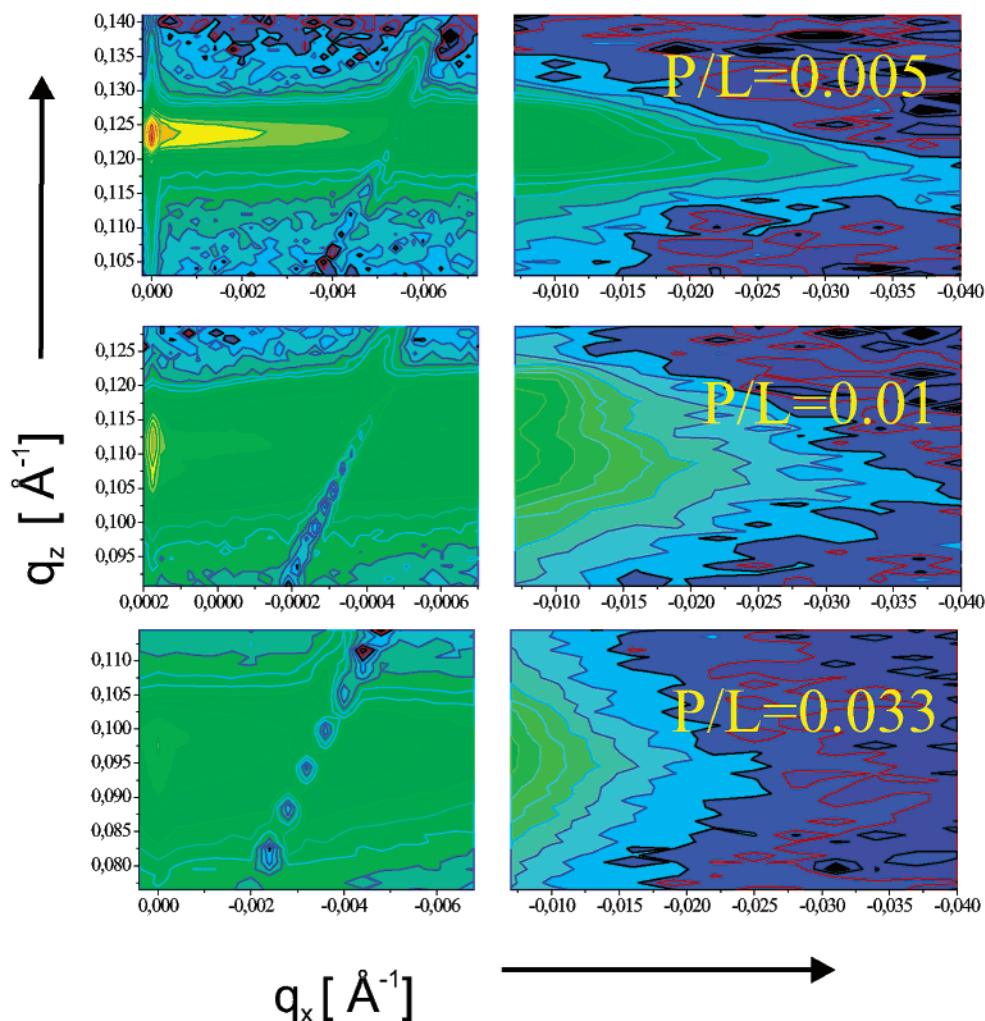
Figure 6. Reciprocal space mappings of the first Bragg sheet as a function of peptide-to-lipid ratio (magainin to DMPC) P/L = 0.005, 0.01, and 0.033, from top to bottom. A distinct broadening of the Bragg sheet in q_z is observed, reflecting significant changes in the fluctuation spectrum with increasing peptide concentration.

decay of the intensities is also evident in the reflectivity curves of increasing P/L, see Figure 7a. A corresponding disordering of the lamellar structure, possibly due to both thermal fluctuations and static defects, is observed at high P/L. As expected, the disordering affects the higher order Bragg sheets most strongly but also reduces the first Bragg sheet, as seen in Figure 6 and Figure 7a. At the highest concentration of P/L = 0.1, all Bragg peaks have vanished, indicating a loss of the multilamellar structure. The decay of the specular Bragg peaks and the diffuse (nonspecular) Bragg sheets is accompanied by a swelling of the lamellar stack with P/L, that is, an increase in d. This is probably due to electrostatic repulsion of the lamellae stemming from the increasing surface charge density, since each peptide carries about 4−5 net charges at neutral pH.

It is interesting to quantify the decrease of lamellar ordering. The obvious approach would be to evaluate the parameters of the smectic model, B and Λ, as a function of P/L. To this end, data such as the reciprocal space mappings shown in Figure 6 have been collected. However, the analysis shows that the smectic model can no longer be used to describe the data of the peptide−lipid systems. This is illustrated in Figure 7b, which shows the HWHM$_{q_z}$-($q_{||}$) curves, evaluated from the reciprocal space mappings in Figure 6. Only for P/L = 0 can we observe the characteristic parabolic increase in the HWHM values. For higher P/L, the width of the Bragg sheet becomes larger but approximately constant as a function of q_x, apart

from the refraction effects observed at the transition zone where α_i changes sign. Note that the values of q_x, where the results are spoiled by the refraction effects, occur at different values for each P/L due to the corresponding changes in d. But already from the small q_x values it is clear that an appropriate theoretic model is lacking to account for the changes in the diffuse scattering with P/L. These changes reflect the lamellar disorder induced by the peptides, including both static defects and thermal fluctuations. As an experimental result, we clearly see that the cross-correlation length decreases, that is, that the bilayers are less correlated in their respective deviations from the flat reference state. At the same time, we stress that not all lipid−peptide systems show such dramatic changes in the reflectivity with P/L, which differ with the peptide and the lipid component. Possibly, the preparation procedure (choice of organic solvent, wetting film) may lead to samples of very different defect structures and thus also different reflectivity signals.

VI. Conclusions and Summary

These results of the previous section show that non-specular scattering may be used as a tool to elucidate lipid−peptide interaction on the basis of changing fluctuation and elasticity properties. To this end, an appropriate model is needed. Turner and Sens have explored the statistical physics of particle inclusions in smectic liquid crystals,[41] providing a quantitative description of
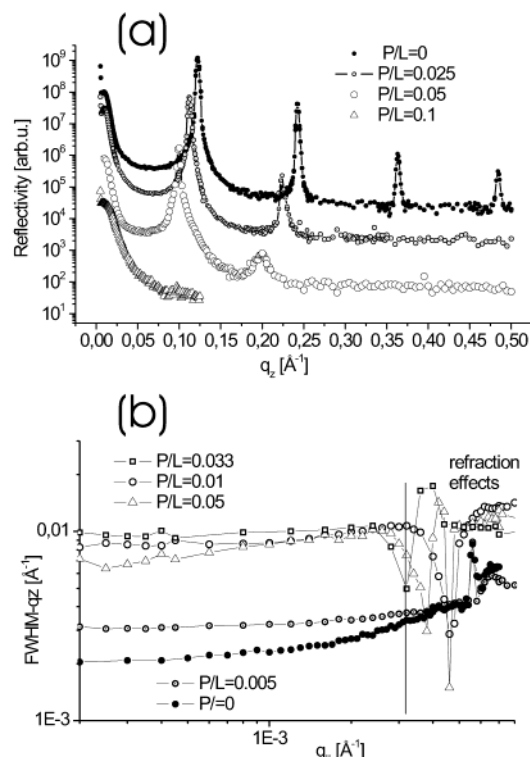
Figure 7. (a) Specular reflectivity curves of increasing peptide-to-lipid ratio (magainin to DMPC) P/L = 0, 0.025, 0.05, and 0.1, from top to bottom (shifted for clarity). The decrease of the higher order peaks with P/L indicates a growing fluctuation amplitude σ. (b) The increase of the Bragg sheet width HWHM along q_x as a function of q_x, for P/L = 0, 0.005, 0.01, and 0.033, evaluated from the reciprocal space mappings of Figure 6, quantifying the broadening of the Bragg sheet with P/L.

the deformation fields around static defects, as caused by inclusions. Their model, however, is based on the smectic model, and the inclusions lead to effective smectic parameters which change as a function of P/L, while the present data show that the scattering distribution can no longer be described by Caillé theory. A generalized theory with corresponding parameters is still lacking and could stimulate the further use of nonspecular reflectivity. The present results also show that pronounced changes of the fluctuation spectrum occur already at moderate peptide concentration, for example, at P/L = 0.005, where the changes in the specular reflectivity are still quite small. We speculate that the lipid−peptide interaction at moderate concentration is physiologically more relevant than the interaction at higher concentrations which may not be reached in biological systems.

For the case of pure DMPC, in the fluid phase at $T \simeq$ 40 °C we have found values of $\lambda = 32$ Å and $\sigma = 8.4$ Å (from the fit of Figure 3). The errors for both values are estimated to be on the order of 10%. Note the proportionality $\sigma^2 \propto \eta$. The expression for $g(r)$ following eq 2 shows that the corresponding proportionality constant depends on the largest lateral length scale ξ_{max}. Note also that the result on Λ is based on the assumption that the parabolic broadening of the diffuse Bragg sheet is governed by a

prefactor $\Lambda_x = (\sqrt{2})\Lambda$, if the diffuse scattering is integrated over one direction (i.e., in the present case along y, perpendicular to the xz-scattering plane). Due to computational difficulty, we could not rigorously derive the prefactor $\sqrt{2}$ but found it numerically for a reasonable special choice of $S(\mathbf{q})$.[39] Furthermore, the following problems are associated with the verification of the parabolic law HWHM$_{q_z}(q_x)$ predicted for smectics: (i) First, the width saturates for $q_x \geq 0.01$ Å^{-1}, pointing to contributions from collective molecular motions which are distinct from bending. (ii) Second, the initial increase in the curve shows some spread and may also be explained by functions other than parabolas. Point i is accompanied by corresponding deviations from the smectic model in the curve $S(q_x)$ also observed at high q_x, see Figure 3. We speculate that collective protrusion of peristaltic modes of the bilayers is at the origin of this observation, but a $q_{\parallel}$-dependent κ could also explain this finding. Importantly, the comparison with model curves should be extended to the precise form calculated for films on flat substrates,[26] rather than for bulk smectics. We stress, however, that the present results have been verified by different samples and show consistency between two completely different modes of the experiments, monochromatic and TOF. The TOF mode is very attractive because no motors have to be moved during the scan, and there is an associated gain in measuring time. However, more control is needed concerning the resolution effects in TOF mode. To this end, suitable techniques of measuring the resolution, that is, the intrinsic width of the cross sections (cuts) along λ for constant angles 2θ, have to be developed, to verify the resolution model according to ref 37.

Only a few limited methods are currently available to determine the fundamental smectic length scale Λ or the bilayer bending rigidity κ. While light scattering or optical microscopy techniques determine κ from thermal fluctuations on much larger length scales, which may lead to different values, X-ray powder diffraction and line shape analysis is sensitive to Λ only in the limit of very soft and strongly undulating systems, untypical for phospholipids. By nonspecular neutron and X-ray scattering from aligned phases, the bilayer structure and fluctuation are accessible over a wide range both for relatively stiff and soft systems, covering length scales from the molecular scale up to a few hundreds of nanometers. Despite the remaining questions related to different technical aspects, we hope that the present work stimulates further use and development of the TOF-mode nonspecular scattering technique, suitable for many different problems related to interfacial fluctuations or roughness.